ChemComm

COMMUNICATION

View Article Online
View Journal | View Issue

Cite this: *Chem. Commun.*, 2023, 59, 3711

Received 5th January 2023,
Accepted 1st March 2023

DOI: 10.1039/d3cc00044c

rsc.li/chemcomm

One-dimensional organic metal halide nanoribbons with dual emission†

Sujin Lee,[a] Rijan Karkee,[b] Azza Ben-Akacha,[a] Derek Luong,[c] J. S. Raaj Vellore Winfred,[a] Xinsong Lin,[a] David A. Strubbe *[b] and Biwu Ma *[a]

Organic metal halide hybrids with low-dimensional structures at the molecular level have received great attention recently for their exceptional structural tunability and unique photophysical properties. Here we report for the first time the synthesis and characterization of a one-dimensional (1D) organic metal halide hybrid, which contains metal halide nanoribbons with a width of three octahedral units. It is found that this material with a chemical formula $C_8H_{28}N_5Pb_3Cl_{11}$ shows a dual emission with a photoluminescence quantum efficiency (PLQE) of around 25%. Photophysical studies and density functional theory (DFT) calculations suggest the coexisting of delocalized free excitons and localized self-trapped excitons in metal halide nanoribbons leading to the dual emission.

Metal halide perovskites and perovskite-related organic–inorganic hybrid materials have emerged as an important class of functional materials for a wide range of applications, including solar cells, light emitting diodes (LEDs), scintillators, *etc.* The exceptional structural tunability of this class of hybrid materials *via* the control of both organic and metal halide components has led to the development of a variety of low dimensional structures at the molecular level, ranging from quasi-two dimensional (2D) to layered-2D, corrugated-2D, one-dimensional (1D), and zero-dimensional (0D) structures.[1] Due to the isolation of metal halides by organic components, different degrees of electronic band formation and structural distortion can be achieved in these materials, which exhibit unique optical and electronic properties different from those of 3D metal halide perovskites.[2] For instance, narrowband emissions with small Stokes shifts from free excitons (FEs) are obtained in many quasi-2D and layered-2D metal halide perovskites[3,4] while strongly Stokes-shifted broadband emissions from localized self-trapped excitons (STEs) are recorded in most 1D and 0D organic metal halide hybrids.[5,6] For a few corrugated-2D and 1D organic metal halide hybrids, the coexistence of FEs and STEs can produce multiband white emissions.[2,7]

While early reports on 1D organic metal halide hybrids date back to the 1990s,[8] they have attracted great attention since 2017 with the discovery of 1D $C_4N_2H_{14}PbBr_4$, which exhibits bluish white emission with PLQEs of up to 20%.[7] Dozens of 1D organic metal halide hybrids have been reported since then with improved PLQEs. For instance, Gautier *et al.* reported white emitting 1D $(TDMP)PbBr_4$ with a PLQE of around 45%.[9] More recently, a PLQE of around 60% was recorded in yellowish white-emitting 1D $[C_4N_2H_{12}]_3[PbBr_5]_2{\cdot}4DMSO$.[10] The rich chemistry of organic metal halide hybrids has enabled synthesis of diverse 1D structures containing corner-, edge-, and face-sharing metal halides. In addition to 1D linear chains, corrugated and tubular 1D structures have been assembled using metal halides.[11,12] The different 1D structures lead to distinct optical properties, with some showing dual emissions from both FEs and STEs and others exhibiting strongly Stokes-shifted broadband emissions from STEs only. The recent advances in 1D organic metal halide hybrids suggest that there is ample room to develop new types of 1D structures.[5] One classic 1D structure that has not been explored for metal halides is 1D ribbons. Like using benzene rings as building block for the formation of 1D graphene nanoribbons,[13] we hypothesize that 1D metal halide nanoribbons could be prepared using metal halide polyhedra as building block.

Here we report for the first time the synthesis and characterization of a 1D organic metal halide hybrid, $C_8H_{28}N_5Pb_3Cl_{11}$, containing metal halide nanoribbons with a width of three octahedral units. In this unique 1D hybrid, the corner- and edge-sharing octahedral lead chloride chains $(Pb_3Cl_{11}^{5-})_\infty$ are encompassed by long multiply charged organic tetraethylenepentammonium cations ($TEPA^{5+}$, $C_8H_{28}N_5^{5+}$). Greenish-white

[a] *Department of Chemistry and Biochemistry, Florida State University, Tallahassee, Florida, 32306, USA. E-mail: bma@fsu.edu*
[b] *Department of Physics, University of California, Merced, Merced, CA, 95343, USA. E-mail: dstrubbe@ucmerced.edu*
[c] *Department of Biology Science, Florida State University, Tallahassee, Florida, 32306, USA*

† Electronic supplementary information (ESI) available: Detailed experimental materials and characterizations can be found in the supplementary information. CCDC 2244486. For ESI and crystallographic data in CIF or other electronic format see DOI: https://doi.org/10.1039/d3cc00044c

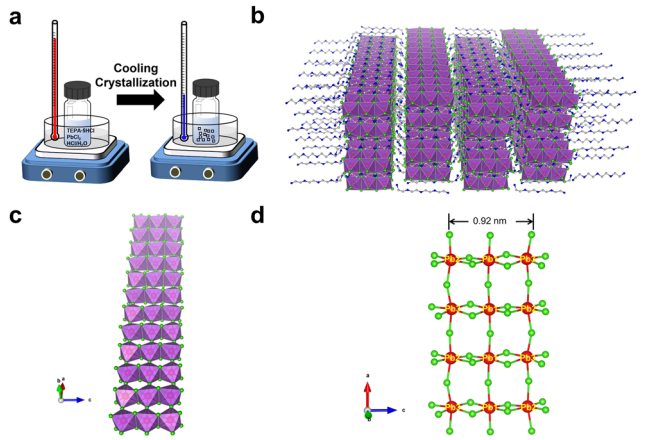

Fig. 1 (a) Synthetic scheme for the material preparation; (b) crystal structure of $C_8H_{28}N_5Pb_3Cl_{11}$ (grey spheres, carbon atoms; blue spheres, nitrogen atoms; red spheres, lead atoms; green spheres, chloride atoms; hydrogen atoms and oxygen atoms were hidden for clarity); (c) view of a lead chloride nanoribbon; (d) ball-and-stick model of a lead chloride nanoribbon.

light emission with peaks at around 420 nm and 540 nm is observed under UV light irradiation (365 nm) at room temperature, with a PLQE of around 25%.

$C_8H_{28}N_5Pb_3Cl_{11}$ single crystals were prepared by gradually cooling a hydrochloric acid solution of tetraethylenepentamine pentahydrochloride (TEPA·5HCl) and lead chloride ($PbCl_2$) (Fig. 1a). The crystal structure of colorless thin plate-like single crystals was determined by single-crystal X-ray diffraction (SCXRD), which shows a structure with orthorhombic space group *Pbca*. Detailed structural analysis can be found in the ESI† (Table S1). The uniformity and structural phase consistency of 1D $C_8H_{28}N_5Pb_3Cl_{11}$ single crystals were confirmed by powder XRD (Fig. S1, ESI†). Although $C_8H_{28}N_5Pb_3Cl_{11}$ single crystals were found to contain a small amount of water molecules (~1.5%), as confirmed by thermogravimetric analysis (Fig. S2, ESI†) and elemental analysis (see details in the ESI†), computational studies suggest that such O-containing impurities (H_2O) have little-to-no effect on their structural properties, and a minimum effect on the optical properties, primarily an increase in absorption at shorter wavelengths for *x*-polarization (Fig. S3, ESI†).

The novel 1D structure at the molecular level is depicted in Fig. 1b, in which anionic metal halide nanoribbons $(Pb_3Cl_{11}^{5-})_\infty$ are isolated and surrounded by multi-charged organic cations $C_8H_{28}N_5^{5+}$. For an individual metal halide nanoribbon (Fig. 1c), metal halide octahedra ($PbCl_6^{4-}$) are connected *via* both corner-sharing in the long *a*-direction and edge-sharing in the short *c*-direction, unlike corner-sharing only as in typical layered-2D perovskites.[14] The width of an individual nanoribbon with three metal halide octahedral units is about 0.92 nm, which is significantly smaller than the typical Bohr exciton radius of metal halide perovskites (~7 nm),[15] suggesting strong quantum confinement in two dimensions. As shown in many previous studies, the geometry and charge of organic cations play an essential role in controlling the formation of low dimensional metal halides.[16,17] The nanoribbon structure here is indeed enabled by organic cations $C_8H_{28}N_5^{5+}$, where the length of an organic cation (~14 Å) is similar to that of three metal halide octahedral units (~12 Å). Also, the distance between nearby ammonium groups (~3.8 Å) is similar to the length between two chloride atoms along the octahedral edge (~3.8–4.2 Å), allowing ammonium groups to bind closely with chloride atoms to form a layer of organic cations on metal halide nanoribbons.

Structural distortion is an important characteristic of metal halides, which affects the formation of STEs and subsequently the photophysical properties. For 1D $C_8H_{28}N_5Pb_3Cl_{11}$, three types of metal halide octahedra ($PbCl_6^{4-}$) with different degrees of structural distortions are present in an individual nanoribbon (Fig. 1d). To quantify the structural distortions, we have calculated the distortion of each $PbXCl_6^{4-}$ (X = 1, 2, and 3) octahedron according to the formula $\Delta_{oct} = \frac{1}{6}\sum_i \left(\frac{d_i - d_{avg}}{d_{avg}}\right)^2$,[18] in which d_i is the distance of each Pb–Cl bond and d_{avg} is the average Pb–Cl bond distance. $Pb1Cl_6^{4-}$ is located in the middle of the ribbon, linking both $Pb2Cl_6^{4-}$ and $Pb3Cl_6^{4-}$. The Pb1–Cl bond lengths range from 2.821 to 2.956 Å and Δ_{oct} of $Pb1Cl_6^{4-}$ is 2.4×10^{-4}. $Pb2Cl_6^{4-}$ and $Pb3Cl_6^{4-}$, located on both sides of the metal halide nanoribbon along the *a*-axis, are highly distorted compared to $Pb1Cl_6^{4-}$, giving Δ_{oct} of 20.0×10^{-4} and 19.0×10^{-4}, respectively, with Pb–Cl bond lengths ranging from 2.705 to 3.114 Å in $Pb2Cl_6^{4-}$ and from 2.734 to 3.085 Å in $Pb3Cl_6^{4-}$. Metal halide distortions of this magnitude have been found to lead to the formation of STEs.[2,12]

The photophysical properties of $C_8H_{28}N_5Pb_3Cl_{11}$ are characterized *via* both steady-state and time-resolved spectroscopies. As shown in Fig. 2a, 1D $C_8H_{28}N_5Pb_3Cl_{11}$ single crystals are colorless under ambient light and exhibit greenish-white emission upon ultraviolet (UV) irradiation (365 nm). The excitation and emission spectra of $C_8H_{28}N_5Pb_3Cl_{11}$ are shown in Fig. 2b.

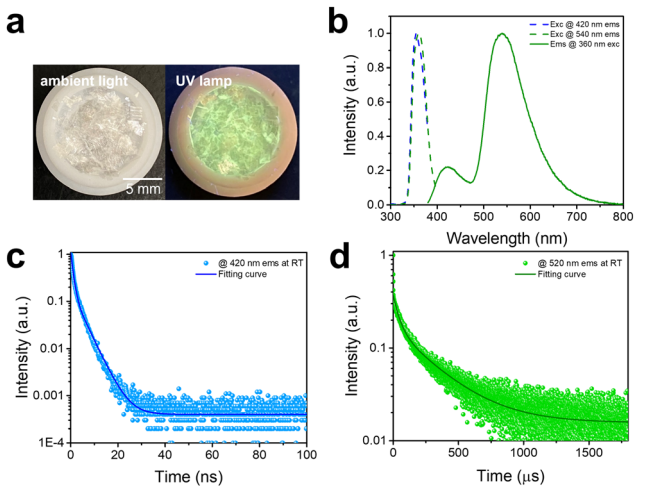

Fig. 2 (a) Images of $C_8H_{28}N_5Pb_3Cl_{11}$ single crystals under ambient light (left) and under UV (right); (b) excitation and emission spectra of $C_8H_{28}N_5Pb_3Cl_{11}$ single crystals at room temperature; (c) photoluminescence decay for the emission peaked at 420 nm; (d) photoluminescence decay for the emission peaked at 540 nm.

A dual emission with a PLQE of 25% (Fig. S4, ESI†) is recorded, whereas the high-energy emission band peaked at around 420 nm has a full width at half maximum (FWHM) of ~60 nm (~0.46 eV) and the low-energy emission band peaked at around 540 nm has a FWHM of ~100 nm (~0.41 eV). The excitation spectra (Fig. 2b) for peak emissions at 420 nm and 540 nm are found to be almost identical, and located at the absorption band edge (Fig. S5, ESI†), suggesting that both emissions originate from the same initially excited state. Room-temperature time-resolved photoluminescence spectra for peak emissions at 420 nm and 540 nm are shown in Fig. 2c and d, giving decay lifetimes of ~1.8 ns and ~250 μs, respectively. Considering that similar dual emissions have previously been observed in corrugated-2D and 1D organic metal halides where FEs and STEs coexist,[7] it is reasonable to attribute the high-energy emission to FEs and the low-energy emission to the STEs in this 1D $C_8H_{28}N_5Pb_3Cl_{11}$. Unlike many previously reported systems, showing similar decay lifetimes for the emissions from FEs and STEs due to thermal equilibrium at RT,[7] 1D $C_8H_{28}N_5Pb_3Cl_{11}$ shows completely different decay behaviors for FEs and STEs (Fig. S6, ESI†), suggesting that emitting states are not in thermal equilibrium in this system. In other words, at short times after the excitation, excitons are distributed between FEs and STEs without de-trapping from STEs to FEs. This behavior is indeed similar to that observed in many molecular systems exhibiting both fluorescence and phosphorescence.[19]

To further clarify the intrinsic nature of the two emission bands, we have measured the dependence of emission intensity on excitation power density at room temperature (Fig. 3a). The intensities of both emission bands show a linear dependence on the excitation power density, suggesting that both emissions are intrinsic properties rather than from defects.[20] Furthermore, to exclude an origin of emissions from permanent defects on the surface that often occur in conventional semiconducting materials such as CdSe, we have compared the emission spectra of bulk single crystals and ground powder of $C_8H_{28}N_5Pb_3Cl_{11}$ with the particle sizes of less than 3 μm.[21] The almost identical emissions from single crystals and ground powder (Fig. S7, ESI†) confirm no significant emission from surface defects. Low-temperature photophysical properties were also characterized for 1D $C_8H_{28}N_5Pb_3Cl_{11}$ at 77 K. Like most low-dimensional organic metal halide hybrids, only strongly Stokes-shifted broadband emission peaked at ~580 nm from STEs is recorded at 77 K (Fig. 3b) with a decay lifetime of around 4.6 μs (Fig. 3c). Considering the distinct photophysical properties at RT and 77 K, we believe that the key photophysical processes could be depicted as in Fig. 3d. At room temperature, upon photoexcitation, 1D $C_8H_{28}N_5Pb_3Cl_{11}$ generates both FEs and STEs without detrapping, resulting in two emissions with different decay dynamics. At 77 K, fast exciton self-trapping leads to a broadband emission from STEs only.

To gain a better understanding of the structure–property relationship for 1D $C_8H_{28}N_5Pb_3Cl_{11}$, we have performed plane-wave DFT calculations (see details in the ESI†). Relaxation starting from the SCXRD structure (a = 11.35 Å, b = 15.85 Å, c = 32.12 Å, $\alpha = \beta = \gamma = 90^\circ$) gave lattice parameters in close agreement (a = 11.32 Å, b = 15.85 Å, c = 32.15 Å, $\alpha = \beta = \gamma = 90^\circ$), as in work on other materials.[22] The calculated electronic band structure of $C_8H_{28}N_5Pb_3Cl_{11}$ is shown in Fig. 4a; the gap is direct and computed to be 3.24 eV. This is close to, though slightly less than, the experimental result from Tauc fitting (Fig. S8, ESI†), in accordance with the common cancellation of errors between neglect of spin–orbit coupling and quasiparticle corrections in hybrid perovskites.[23] The valence band maximum (VBM) has contribution mostly from p-orbitals of Cl and C, whereas at the conduction band minimum (CBM), p-orbitals of Pb dominate (Fig. 4b and c). The electronic bands are dispersive along the Pb–Cl chain direction (x), with effective

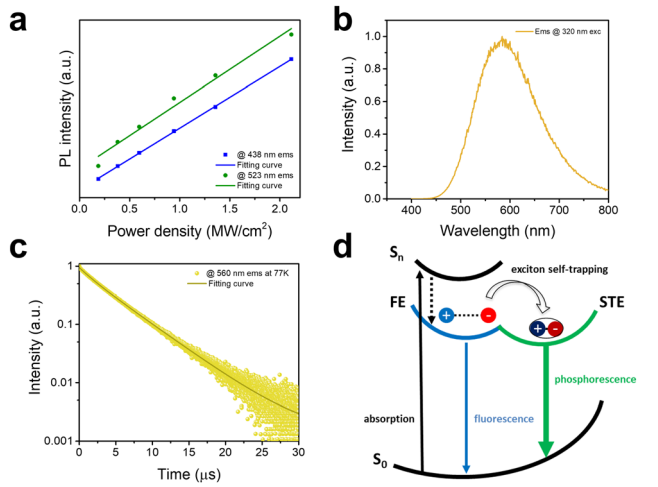

Fig. 3 (a) Excitation power-dependent photoluminescence; (b) emission spectra of $C_8H_{28}N_5Pb_3Cl_{11}$ single crystals at 77 K; (c) photoluminescence decay at 77 K; (d) schematic photophysical processes in $C_8H_{28}N_5Pb_3Cl_{11}$.

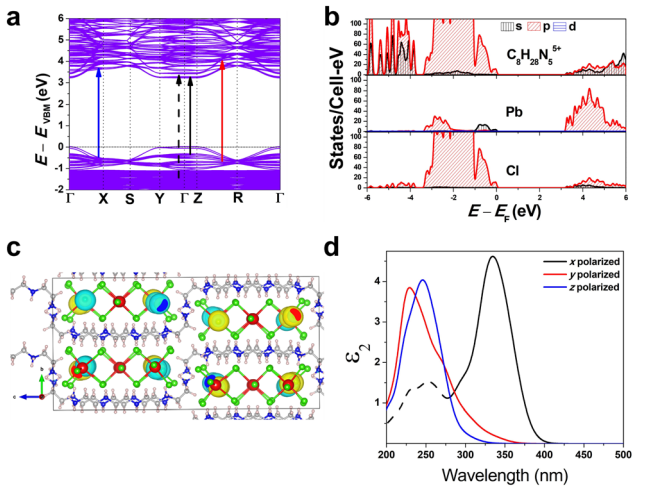

Fig. 4 Density-functional theory simulations: (a) electronic band structure, with arrows showing optical transitions for peaks polarized along x (black), y (red), and z (blue) directions, where x is the direction along the Pb–Cl chains, and the solid and dotted black arrows indicate the lowest and second-lowest energy x-polarized peaks; (b) partial density of states; (c) wavefunction of the conduction band minimum at Γ, localized along the Pb–Cl chains; (d) polarized absorption spectra, where the x-polarized peaks are solid and dotted as in (a).

masses at the Γ point of $m^*_{VBM} = -0.34\ m_0$ and $m^*_{CBM} = 0.09\ m_0$, but are nearly flat along other two perpendicular directions (*y*: $m^*_{VBM} = -2.25\ m_0$, $m^*_{CBM} = 4.23\ m_0$; *z*: $m^*_{VBM} = -18.5\ m_0$, $m^*_{CBM} = 12.5\ m_0$) as shown in Fig. 4a.

Additionally, we have calculated the absorption (see details in the ESI†) shown in Fig. 4d. The first absorption peak is strong along the Pb–Cl chain (*x*-polarized), suggesting that the electronic transition in the band edges is coming from the Pb–Cl chain. For *x*-polarization, the strong transition is due to VBM-8 and VBM-7 to CBM+4 bands (very close in energy to VBM to CBM transitions). This calculated direct absorption peak matches well with our experimental absorption results (Fig. S5 and S8, ESI†). Similarly for *y*-polarization, a transition from VBM-17 to CBM+47 bands dominates; and for *z*-polarization, from VBM-21 to CBM+27 bands. Furthermore, Fig. 4d shows strong anisotropy in absorption. These calculations indicate that the FE emission comes from the recombination of excitons on the Pb–Cl chain. The experimental emission energy for both emitting states should be lower than the bandgap due to the strong exciton binding as usual in low-dimensional structures, as well as Stokes shifts. We also constructed an analogous bulk structure containing 2D sheets of Pb–Cl atoms in plane (Fig. S9, ESI†), separated by organic molecules out of plane, and obtained a bandgap of 2.84 eV. The orbital nature of the band edges is similar to 1D $C_8H_{28}N_5Pb_3Cl_{11}$. This suggests a quantum confinement effect of 0.40 eV in this material as one goes from 2D to 1D.

In conclusion, we have developed a novel 1D organic metal halide hybrid ($C_8H_{28}N_5Pb_3Cl_{11}$) consisting of metal halide nanoribbons with a width of three octahedral units. 1D $C_8H_{28}N_5Pb_3Cl_{11}$ is found to exhibit a dual emission with a high energy emission peaked at 420 nm and a low energy broad emission peaked at 540 nm, due to the coexistence of free excitons and self-trapped excitons. Our work further advances research on low dimensional organic metal halide hybrids with a unique nanoribbon structure, which bridges between linear chain 1D structures and layered-2D structures. It shows once again the exceptional tunability of organic metal halide hybrids, which could lead to the further development of this class of functional hybrid materials for many applications.

The work is mainly supported by the National Science Foundation (NSF) (DMR-2204466). It made use of a Rigaku Synergy-S single-crystal X-ray diffractometer which was acquired through the NSF MRI program (CHE-1828362), as well as a nanosecond-transient absorption spectrometer which was acquired through the NSF MRI program (CHE-1531629). Computational work was supported by the Air Force Office of Scientific Research under the award number FA9550-19-1-0236. Computational resources were provided by the Multi-Environment Computer for Exploration and Discovery (MERCED) cluster at UC Merced funded by NSF (ACI-1429783).

Conflicts of interest

There are no conflicts to declare.

Notes and references

1 C. Zhou, H. Lin, Q. He, L. Xu, M. Worku, M. Chaaban, S. Lee, X. Shi, M.-H. Du and B. Ma, *Mater. Sci. Eng., R*, 2019, **137**, 38–65.
2 M. D. Smith, E. J. Crace, A. Jaffe and H. I. Karunadasa, *Annu. Rev. Mater. Res.*, 2018, **48**, 111–136.
3 Z. Yuan, Y. Shu, Y. Xin and B. Ma, *Chem. Commun.*, 2016, **52**, 3887–3890.
4 X. Li, J. M. Hoffman and M. G. Kanatzidis, *Chem. Rev.*, 2021, **121**, 2230–2291.
5 M. Z. Rahaman, S. Ge, C.-H. Lin, Y. Cui and T. Wu, *Small Struct.*, 2021, **2**, 2000062.
6 C. Zhou, L.-J. Xu, S. Lee, H. Lin and B. Ma, *Adv. Opt. Mater.*, 2021, **9**, 2001766.
7 Z. Yuan, C. Zhou, Y. Tian, Y. Shu, J. Messier, J. C. Wang, L. J. van de Burgt, K. Kountouriotis, Y. Xin, E. Holt, K. Schanze, R. Clark, T. Siegrist and B. Ma, *Nat. Commun.*, 2017, **8**, 14051.
8 S. Wang, D. B. Mitzi, C. A. Feild and A. Guloy, *J. Am. Chem. Soc.*, 1995, **117**, 5297–5302.
9 R. Gautier, F. Massuyeau, G. Galnon and M. Paris, *Adv. Mater.*, 2019, **31**, e1807383.
10 G. Yu, F. Lin, K. Zhou, S. Fang, Y. Shi, W. Liu, H. Hu, B. Ma and H. Lin, *Chem. Mater.*, 2021, **33**, 5668–5674.
11 H. Lin, M. Green, L.-J. Xu, X. Chen and B. Ma, *Adv. Mater. Interfaces*, 2020, **7**, 1901270.
12 H. Lin, C. Zhou, J. Neu, Y. Zhou, D. Han, S. Chen, M. Worku, M. Chaaban, S. Lee, E. Berkwits, T. Siegrist, M.-H. Du and B. Ma, *Adv. Opt. Mater.*, 2019, **7**, 1801474.
13 R. S. K. Houtsma, J. de la Rie and M. Stohr, *Chem. Soc. Rev.*, 2021, **50**, 6541–6568.
14 K. Z. Du, Q. Tu, X. Zhang, Q. Han, J. Liu, S. Zauscher and D. B. Mitzi, *Inorg. Chem.*, 2017, **56**, 9291–9302.
15 J. Butkus, P. Vashishtha, K. Chen, J. K. Gallaher, S. K. K. Prasad, D. Z. Metin, G. Laufersky, N. Gaston, J. E. Halpert and J. M. Hodgkiss, *Chem. Mater.*, 2017, **29**, 3644–3652.
16 R. Lyu, C. E. Moore, T. Liu, Y. Yu and Y. Wu, *J. Am. Chem. Soc.*, 2021, **143**, 12766–12776.
17 M.-H. Tremblay, A. Boyington, S. Rigin, J. Jiang, J. Bacsa, K. Al Kurdi, V. N. Khrustalev, R. Pachter, T. V. Timofeeva, N. Jui, S. Barlow and S. R. Marder, *Chem. Mater.*, 2022, **34**, 935–946.
18 D. Cortecchia, S. Neutzner, A. R. Srimath Kandada, E. Mosconi, D. Meggiolaro, F. De Angelis, C. Soci and A. Petrozza, *J. Am. Chem. Soc.*, 2017, **139**, 39–42.
19 C. Salas Redondo, P. Kleine, K. Roszeitis, T. Achenbach, M. Kroll, M. Thomschke and S. Reineke, *J. Phys. Chem. C*, 2017, **121**, 14946–14953.
20 G. Wu, C. Zhou, W. Ming, D. Han, S. Chen, D. Yang, T. Besara, J. Neu, T. Siegrist, M.-H. Du, B. Ma and A. Dong, *ACS Energy Lett.*, 2018, **3**, 1443–1449.
21 L. J. Xu, X. Lin, Q. He, M. Worku and B. Ma, *Nat. Commun.*, 2020, **11**, 4329.
22 K. Talit and D. A. Strubbe, *J. Phys. Chem. C*, 2020, **124**, 27287–27299.
23 L. Leppert, T. Rangel and J. B. Neaton, *Phys. Rev. Mater.*, 2019, **3**, 103803.

